

Article

Kinesin-1 Motors Can Circumvent Permanent Roadblocks by Side-Shifting to Neighboring Protofilaments

René Schneider,^{1,2} Till Korten,^{1,2} Wilhelm J. Walter,¹ and Stefan Diez^{1,2,*}¹B CUBE—Center for Molecular Bioengineering, Technische Universität, Dresden, Germany; and ²Max Planck Institute of Cell Biology and Genetics, Dresden, Germany

ABSTRACT Obstacles on the surface of microtubules can lead to defective cargo transport, proposed to play a role in neurological diseases such as Alzheimer's. However, little is known about how motor proteins, which follow individual microtubule protofilaments (such as kinesin-1), deal with obstacles on the molecular level. Here, we used rigor-binding mutants of kinesin-1 as roadblocks to permanently obstruct individual microtubule binding sites and studied the movement of individual kinesin-1 motors by single-molecule fluorescence and dark-field scattering microscopy *in vitro*. In the presence of roadblocks, kinesin-1 often stopped for ~0.4 s before either detaching or continuing to move, whereby the latter circumvention events occurred in >30% after a stopping event. Consequently, and in agreement with numerical simulations, the mean velocity, mean run length, and mean dwell time of the kinesin-1 motors decreased upon increasing the roadblock density. Tracking individual kinesin-1 motors labeled by 40 nm gold particles with 6 nm spatial and 1 ms temporal precision revealed that ~70% of the circumvention events were associated with significant transverse shifts perpendicular to the axis of the microtubule. These side-shifts, which occurred with equal likelihood to the left and right, were accompanied by a range of longitudinal shifts suggesting that roadblock circumvention involves the unbinding and rebinding of the motors. Thus, processive motors, which commonly follow individual protofilaments in the absence of obstacles, appear to possess intrinsic circumvention mechanisms. These mechanisms were potentially optimized by evolution for the motor's specific intracellular tasks and environments.

INTRODUCTION

Efficient and durable transport driven by motor proteins along cytoskeletal filaments is particularly important for neurons, which possess long axonal protrusions (1). Not surprisingly, the impairment of motor motility is speculated to cause neurodegenerative diseases such as Alzheimer's (2,3). There, it is discussed that the anterograde movement of kinesin-1 motors transporting vesicular cargo along individual protofilaments of axonal microtubules (MTs) is strongly affected by permanent obstacles on the MT lattice, markedly before the onset of disease-related pathologies such as amyloid deposition and neurofibrillary tangles (4,5).

Previous *in vivo* studies addressing the motility of motors in the presence of the native neuronal microtubule-associated protein (MAP) tau, showed that the binding frequency and the run length of motor-coupled organelles reduced, whereas the transport velocity was only mildly affected (6); an observation that was reproduced *in vitro* for kinesin-1 coupled to beads (7) or labeled by green fluorescent protein (GFP) (8–10). The recent finding that tau diffuses on MTs *in vitro* (11) delivered an explanation for the mild

effect of tau on kinesin-1 velocity and contributed to the complexity of the tau-MT interaction. Thus, tau cannot be regarded as a purely stationary obstacle and therefore motivated *in vitro* experiments with artificial obstacles that block the motor binding sites permanently. To this end, Crevel et al. (12) used rigor-binding mutants of kinesin-1 to study the unbinding kinetics of active kinesin-1 motors from mutant-saturated MTs. They found that motors detached with a high off-rate of 42 s⁻¹. Such a large rate (only <twofold smaller than the measured stepping rate) indicates that motors must detach shortly after encountering an obstacle, i.e., without any significant waiting phase. Using single-molecule fluorescence microscopy, different observations were made by Telley et al. (13) who found that kinesin-1 has a small, but finite, probability to wait (on average 200–250 ms) upon obstacle encounter. Far longer waiting times were observed by Korten et al. (14), who used streptavidin molecules on biotinylated MTs, and Dreblow et al. (15), who used glutaraldehyde-fixed kinesin (KIF5A) monomers as obstacles. Interestingly, all three of the latter studies mentioned that a small fraction of waiting motors were able to circumvent the blocked positions and continued walking. This observation was taken as indication that kinesin-1 may circumvent obstacles by using binding sites on neighboring protofilaments; a fact speculated about in the literature for years (10,13,15–17). To answer if and how individual motors can circumvent permanent obstacles,

Submitted August 12, 2014, and accepted for publication March 19, 2015.

*Correspondence: diez@bcube-dresden.de

René Schneider's present address is Max Planck Institute of Molecular Plant Physiology, Potsdam-Golm, Germany.

Wilhelm J. Walter's present address is Biozentrum Klein Flottbek, Universität Hamburg, Germany.

Editor: Jennifer Ross.

© 2015 by the Biophysical Society
0006-3495/15/05/2249/9 \$2.00



we used rigor-binding kinesin-1 mutants as roadblocks and GFP-labeled kinesin-1 motors to which we loaded 40 nm gold nanoparticles (AuNPs). AuNPs offer an enormous scattering cross section and were previously shown to provide sufficient localization precision to resolve the characteristic 8-nm stepping of individual kinesin-1 motors (18).

MATERIALS AND METHODS

Protein biochemistry

Recombinant protein constructs contained the N-terminal 430 amino acids of the *Rattus norvegicus* kinesin-1 isoform kif5c (19), C-terminally fused to a His-tag or to enhanced GFP and a His-tag. Rigor-binding kinesin-1 constructs (roadblocks) were engineered by introducing a T93N point mutation using a site-directed mutagenesis kit from Stratagene (Santa Clara, CA). Expression in the *Escherichia coli* strain BL21 (DE3) and purification via immobilized metal ion affinity chromatography was performed as described previously (19). Fluorescent MTs were polymerized from 5 μ L of a 1:3 mixture of rhodamine-labeled and unlabeled porcine brain tubulin (total concentration 4 mg/mL) in BRB80 (80 mM potassium PIPES, pH 6.9, 1 mM EGTA, 1 mM MgCl₂) supplemented with 4 mM MgCl₂, 1 mM MgGTP, and 5% dimethyl sulfoxide (DMSO). After 30 min at 37°C, MTs were transferred to room temperature, immediately stabilized by the addition of 10 μ M Taxol dissolved in BRB80 (BRB80T), centrifuged at 160,000 \times g for 5 min, and resuspended in the same volume of BRB80T.

Conjugation of biotinylated GFP-antibodies to streptavidin-coated AuNPs

Antibody-conjugated AuNPs were prepared from 40 nm streptavidin-coated AuNPs (British Biocell International, Cardiff, UK) and biotinylated GFP-antibodies (from MPI-CBG antibody facility, batch number 106A20) using a protocol described previously (18). Antibody-conjugated AuNPs were used within 1 day after preparation. Loading of antibody-conjugated AuNPs to GFP-labeled motors was performed by incubating both at molar ratios ranging from 10:1 to 1:1 for 15 min on ice. To assure single-molecule conditions always the lowest ratio that still produced moving AuNPs was used (see proofs for single-molecule conditions in Supporting Material D). GFP-antibodies did not interact with unlabeled roadblocks. This was tested in two ways. 1) In the geometry of gliding motility assays, we used surface-bound GFP-antibodies to potentially tether unlabeled roadblocks to the surface. No MTs were observed to land on such surfaces. 2) In the geometry of stepping motility assays, we incubated antibody-conjugated AuNPs with unlabeled roadblocks. No AuNPs were found to colocalize with surface-immobilized MTs. Due to the large size of the AuNPs (~50 antibodies theoretically fit on the particle surface) individual AuNPs may be capable of picking up additional, yet unbound, motors during movement. To reduce the probability of such pick-up events, we used a low total concentration of motors (~150 pM) generating well-separated single-molecule trajectories of moving GFP-labeled kinesin-1 motors.

Microscopic flow-cell experiments

Experiments were performed in flow cells constructed from hydrophobic glass coverslips separated by stripes of double-sided sticky tape as described previously (18). The standard buffer in the experiments was BRB80 supplemented with 1 mM MgATP. For stepping motility assays we used a protocol published previously (18). Briefly, the channels of a flow cell were prepared using the following sequential treatment. 1) Incubation with 0.5% β -tubulin antibodies (SAP.4G5, Thermo Fisher Scientific,

Waltham, MA) in phosphate buffered saline (PBS) for 5 min, 2) washing with 20 μ L BRB80, 3) incubation with Pluronic F127 for 15 min, 4) washing with 80 μ L BRB80T, 5) incubation with 10 μ g/mL MTs for 1 min, and 6) washing with 20 μ L BRB80T. To decorate MTs with roadblocks, the flow cell was incubated for 1 min with 0.75–15 nM unlabeled roadblocks in dilution buffer (BRB80 with 1 mM MgATP, 10 mM DTT, 1% Tween20, and 265 μ g/mL Casein) and subsequently washed-out using imaging buffer (265 μ g/mL Casein, 47 mM Glucose, 130 μ g/mL Glucose Oxidase, 24 μ g/mL Catalase, 12 mM DTT, 1% Tween20, and 1 mM MgATP in BRB80T). Finally, 150 pM GFP-labeled motors were flushed into the channel. For the experiments involving AuNP-loaded motors, a premix of GFP-labeled motors and GFP-antibody-conjugated AuNPs was diluted in imaging solution to a final motor concentration of 150 pM and subsequently flushed into the channel.

Total internal reflection fluorescence microscopy and image acquisition

To image the motility of GFP-labeled motors, objective-type total internal reflection fluorescence (TIRF) microscopy was carried out on an inverted AxioObserver equipped with a TIRF-slider system (both from Zeiss, Göttingen, Germany). The slider was fiber-coupled to a 488 nm diode laser (Stradus 488-50, Vortran Laser Technology, Sacramento, CA) and a 532 nm diode-pumped solid-state laser (Cobolt Samba 100 mW, Cobolt AB, Solna, Sweden). The microscope was equipped with a Lumen 200 metal arc lamp (Prior Scientific Instruments, Jena, Germany) to provide fluorescence excitation in epi-illumination. Excitation and detection of fluorescence was achieved using a 63 \times , NA1.46 α Plan-Apochromat oil immersion objective from Zeiss. To image the motility of AuNP-loaded motors, parabolic prism-type TIR dark-field microscopy was carried out by coupling the lasers to a focusing collimator of a custom-built setup (18). Detection of scattered light was achieved using a 63 \times , NA1.2 C-Apochromat water immersion objective from Zeiss. Fluorescence filters: Unless otherwise mentioned we used the following filter sets from Semrock (Lake Forest, IL): 1) for GFP-labeled proteins, BL HC 482/18, BL HC R488, BL HC 520/35 and 2) for rhodamine-labeled MTs, BL HC 520/35, zt 532 RDC from Chroma (Bellows Falls, VT), HC 585/40. Image acquisition: for capturing fluorescence, we used an electron-multiplied charge-coupled device camera (iXon DV 897E, Andor, Belfast, Northern Ireland), whereas, for capturing scattering, we used a water-cooled CMOS camera (Neo sCMOS, Andor) operated in rolling shutter mode for the smallest available region-of-interest (128 \times 128 pixels²). Water-cooling was achieved using an Exos-2.5 liquid cooling system (Koolance, Auburn, WA). Images were acquired in sequential order using MetaMorph imaging software (Molecular Devices, Sunnyvale, CA). The acquisition sequence consisted of 1) a snapshot image of MTs, 2) continuous recording (streaming) for 100 s at 10 frames/s of GFP-labeled motors, and 3) streaming for 10 s at 1000 frames/s of AuNP-loaded motors. For each roadblock condition, we acquired, tracked, and evaluated at least three recordings.

Image analysis

Fluorescence data

MT snapshots and streams of GFP-labeled motors were tracked using FIESTA (20). Tracked motor trajectories (minimum duration: 4 frames) were double-checked by eye to avoid computer misinterpretations. The run length and dwell time of an individual motor was determined by measuring the total distance and the total duration of the motor trajectory (also see Fig. 1 B). For 1410 stopping and starting motors the waiting times were measured manually using the kymograph analysis tool of FIESTA. Under these conditions, the minimum detection threshold for waiting phases was 200 ms (= 2 frames). The velocity of an individual motor was obtained by dividing the run length by the dwell time. The mean

velocity of many motors was obtained by averaging the individual motor velocities. The mean dwell times, mean run lengths, and mean waiting times were obtained by fitting the respective cumulative probability density to an exponential function (21). We corrected the mean run length, mean dwell time, and mean waiting time for photobleaching using a method based on the determination of the bleaching time (22). We determined the bleaching time to 5.8 ± 0.9 s (mean \pm SD, $N = 3$ movies) under conditions, where the motors were immobilized on MTs using AMP-PNP, a nonhydrolyzable ATP analog.

AuNP data

Motility parameters of AuNP-loaded motors were determined similar to the GFP-labeled motors. To avoid systematic errors in the determination of the motility parameters, we rejected motors from the analysis when their attachment or detachment was not captured in the stream (to a vast extent waiting motors, presumably caused by the motors being inactive). The minimum detection threshold for waiting phases was set to 50 ms (50 frames), because the probability of a Poisson stepper advancing with 100 steps/s to wait for ≥ 50 ms is $< 1\%$. To determine the moving and waiting phases of a motor, we first manually selected transition points in the longitudinal displacement versus time plot. Subsequently, a MATLAB script (The MathWorks, Natick, MA) was used to perform linear regressions of the phases between transition points. Exact transition points were determined by finding the intersection of the linear regressions from neighboring phases. The phases were sorted into moving (mean velocity > 100 nm/s) and waiting (mean velocity < 100 nm/s) phases. By projecting the motor trajectory onto the MT axis, we obtained the transverse and longitudinal components of the displacement of a motor relative to the MT. A transverse shift was then defined as the distance of the two regression lines at the transition point (see Fig. 3 B). A longitudinal shift was defined by the difference between the averaged longitudinal displacements of the AuNPs during 10 ms before and 10 ms after the transition, diminished by 4 nm to account for the movement of the motors after the transition (~ 8 nm during 10 ms).

Simulations

Simulations were carried out using a MATLAB-based computer program, which analyzed the resulting motor trajectories similar to the ones obtained experimentally (see Supporting Material B). Multiple roadblock encounters were considered by allowing steppers to run into subsequent roadblocks along the same protofilament. Effects caused by the imaging and tracking process were considered by including temporal averaging due to finite image integration (100 ms), spatial noising due to finite localization precision (30 nm), and a minimum number of frames necessary to define a trajectory (4 frames). The motility parameters used as input for the simulation were obtained from the experiments in the absence of roadblocks.

Determining the roadblock density on MTs and the mean spacing along protofilaments

To determine the roadblock density on MTs, we decorated surface-immobilized MTs with 0.2–15 nM GFP-labeled roadblocks for 1 min and subsequently flushed 150 pM GFP-labeled motors into the channel. Because the fluorescence of the individual roadblocks bleached during the 100-s recording (bleaching time ~ 7.5 s), the brightness and density of the GFP-labeled motors could be quantified only toward the end of the recordings. We used those numbers to normalize the total fluorescence superimposed with the MTs in the first frame to determine the roadblocks density. We obtained a calibration curve, which provided a means to estimate the density of roadblocks on the MTs based on the concentration of roadblocks used during the decoration step (see Fig. S5). To convert the roadblock density along MTs into roadblock spacing along individual protofilaments, we made the following assumptions (for details, see Supporting Material C). 1) Only half the protofilaments, i.e., the protofilaments facing toward the

solution, are accessible for motors. 2) The calibration curve measured with GFP-labeled roadblocks holds true for unlabeled roadblocks. 3) A low amount of intrinsic obstacles, e.g., formed by the antibodies used to bind MTs to the surface, defective tubulin or tubulin-copurified MAPs, is present on the MTs even in the absence of added roadblocks (estimated to be spaced ~ 1.5 μm apart along a protofilament). 4) All GFP-labeled roadblocks were fluorescent.

RESULTS

The presence of roadblocks on MTs leads to deteriorated kinesin-1 motility

We genetically engineered rigor-binding kinesin-1 mutants (henceforth termed roadblocks) by introducing a T93N point mutation into the Walker A domain of a truncated kinesin-1. This mutant is unable to hydrolyze ATP and is thus locked in the ATP state with high affinity to the MT (23). We verified the rigor binding of individual GFP-labeled roadblocks to surface-immobilized, rhodamine-labeled MTs using objective-type TIRF microscopy (24). We found that roadblocks were immobile and stayed irreversibly bound, even in the presence of actively stepping kinesin-1 motors (henceforth termed motors, see Supporting Material A and Fig. S1). To quantify how these roadblocks affect motor motility, we performed stepping motility assays of GFP-labeled motors on surface-immobilized MTs, which were decorated with variable concentrations of unlabeled roadblocks (Fig. 1 A and Materials and Methods).

The presence of roadblocks had pronounced effects on the motility of individual motors (Fig. 1 B), the trajectories of which contained moving phases (when the motors moved at full velocity) and waiting phases (when the motors appeared statically bound). Depending on the temporal sequence in which moving and waiting phases occurred, we classified the motors into moving (only one single moving phase), waiting (only one single waiting phase), stopping (a moving phase followed by a waiting phase), starting (a waiting phase followed by a moving phase), or pausing (a moving phase followed by a waiting phase followed by another moving phase). In the absence of roadblocks, 82% of the motors were moving, 8% were stopping, 2% were starting, 4% were pausing, and 4% were waiting ($N = 382$). The occurrence of stopping events in the absence of added roadblocks is attributed to a low amount of intrinsic obstacles, e.g., formed by the antibodies used to immobilize the MTs, defective tubulin dimers or tubulin-copurified MAPs. In contrast, at a roadblock concentration of 15 nM, only 17% of the motors were moving, 21% were stopping, 9% were starting, 8% were pausing, and 45% were waiting ($N = 283$). Independent of the degree of roadblock decoration, the time individual motors spent in waiting phases lasted 0.39 ± 0.09 s (mean \pm SD, $N = 1410$, Fig. 1 C). Interestingly, the probability of starting events averaged over experiments performed at seven different roadblock concentrations between 0 and 15 nM was as high as

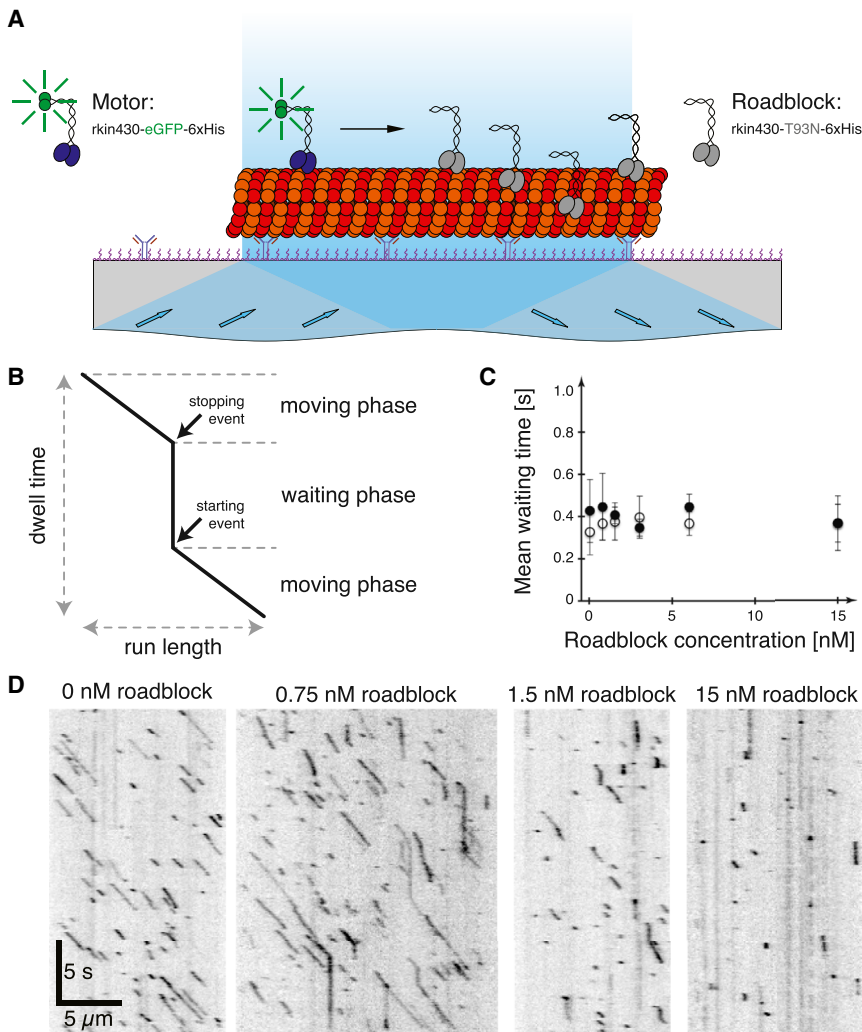


FIGURE 1 Motility of GFP-labeled motors in the presence of unlabeled roadblocks studied by TIRF microscopy. (A) Schematic illustration of the stepping assay and the engineered protein constructs. (B) Definition of the motility parameters. The total distance and the duration of the trajectory were termed run length and dwell time, respectively. Switches from a moving to a waiting phase were termed stopping events. Switches from a waiting to a moving phase were termed starting events. The velocity of an individual motor was obtained by dividing the run length by the dwell time. (C) Mean waiting times of stopping and waiting motors (open circles, 0.37 ± 0.09 s, mean \pm SD, $N = 6$ roadblock concentrations) were similar to the mean waiting times of pausing and starting motors (black spheres, 0.41 ± 0.09 s). (D) Kymographs of individual motors (at 1 mM ATP) walking along MTs decorated by the presence of 0, 0.75, 1.5, and 15 nM roadblock concentration. To see this figure in color, go online.

$28 \pm 5\%$ (mean \pm SD, see also Fig. 1 D and Table S1). Taken together, these results suggest that motors are capable of circumventing a roadblock after a finite waiting phase.

To study how the presence of roadblocks affects the mean velocity, mean run length, and mean dwell time of individual kinesin-1 motors (see Fig. 1 B for the definition of these motility parameters), we used the open-source tracking software FIESTA (20). We found that all three quantities decreased significantly upon increasing the roadblock concentration (Fig. 2, A–C, black symbols, Fig. S2). To investigate whether our measured waiting time (~ 0.4 s) and circumvention probability ($\sim 30\%$, Fig. 2 Di) are sufficient to explain this behavior, we compared our experimental results to numerical simulations where the motors were treated as random steppers advancing along roadblock-decorated MT protofilaments (Materials and Methods, Supporting Material B, and Fig. S3). Simulations were carried out at varying roadblock spacings (Fig. S4) and took the performance of our imaging setup (e.g., the limited spatiotemporal accuracy in imaging single GFP molecules) into account (Materials and Methods).

We found that our simulation (scenario *i*) well reproduced the experimentally determined mean velocities, mean run lengths, and mean dwell times as functions of the roadblock concentration (Fig. 2, A–C, compare the green symbols and lines to the black symbols). Reducing the circumvention probability to 0% (Fig. 2 Dii) did not significantly alter the mean velocities nor the mean run lengths, but produced mean dwell times that were significantly shorter than the measured values (Fig. 2, A–C, compare the orange symbols and lines to the black symbols). Additionally, reducing the waiting time to 0 s (Fig. 2 Diii) did not alter the mean run lengths significantly (see Supporting Material B for details) but further decreased the mean dwell times. Moreover, in contrast to the measured values, in this scenario the mean velocities were predicted to stay high, virtually independent of the roadblock concentration (Fig. 2, A–C, compare the red symbols and lines to the black symbols). Taken together, our simulations show that a finite waiting time and a finite circumvention probability are necessary and sufficient to quantitatively explain our experimental data.

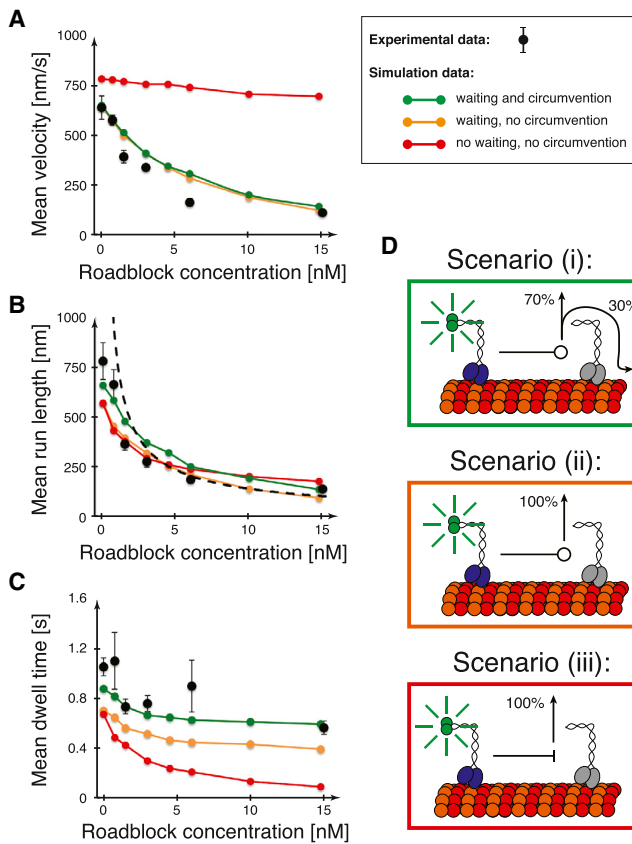


FIGURE 2 Experimental and simulated motility parameters in the presence of roadblocks. (A–C) Deterioration of the motility parameters mean velocity (A), mean run length (B), and mean dwell time (C), as a function of the roadblock concentration (*black dots*, mean \pm SD, $N = 3$ movies with >250 motors total) and comparison with simulated data (*red, orange, and green data points* according to the scenarios in (D), mean \pm SD, $N = 3$ simulations with 1000 motors each). The dotted line in (B) represents the experimentally determined mean roadblock spacing (see [Supporting Material C](#) and [Fig. S5](#)). (D) Simulated roadblock-encounter scenarios: (i) waiting and circumvention: motors wait for 0.4 s and subsequently continue in 30% and detach in 70% of the encounters (*green box*); (ii) waiting and no circumvention: motors detach after 0.4 s of waiting (*orange box*); (iii) no waiting and no circumvention: motors immediately detach upon roadblock encounter (*red box*).

Motors circumvent roadblocks by unbiased side-shifting to the left or right

To investigate the mechanism by which the motors do circumvent roadblocks, we increased the localization precision of the GFP-motors by labeling them with 40 nm AuNPs and imaging them by dark-field microscopy ([Fig. 3 A](#), [Materials and Methods](#)). This way, the localization precision improved to 4.5 nm along and 6.1 nm perpendicular to the MT axis, respectively, within 1 ms imaging time ([Fig. S6](#)). Two-dimensional trajectories of AuNP-loaded motors were then projected onto the MT centerline using FIESTA ([20](#)). Single-molecule conditions, i.e., conditions under which AuNP transportation was driven by individual motors, were ensured by optimizing the incubation ratios of AuNPs

to motors such that the motility parameters of loaded and unloaded motors in the absence and presence of roadblocks were the same ([Supporting Material D](#), [Fig. S7](#), and [Table S2](#)). This approach provided a 95% confidence that individual motors transported AuNPs and that the motility parameters of the motors were unaffected by the AuNPs.

We focused on pausing motors (which occurred on average in 27% of all imaged trajectories obtained at 0 nM, 2 nM, and 4 nM roadblocks, [Table S3](#)) and measured the transverse shifts, i.e., the differences in the transverse displacement of the AuNP from the MT centerline before and after the stopping and starting events ([Fig. 3 B](#), [Material and Methods](#)). Transverse shifts larger than the shift error (sum of the 95% confidence intervals of the transverse displacements before and after the transition point) were considered significant. An exemplary trajectory captured at 2 nM roadblocks ([Fig. 3 C](#)), shows two short waiting phases (90 and 55 ms) with subsequent transverse shifts toward the right (see also [Fig. S8](#) for more examples).

To quantify the transverse shifts, 106 pausing motors were pooled into one evaluation. We observed that in 90% of the stopping events, the motors switched into the waiting phase without a significant transverse shift ([Figs. 3 C](#) and [S8, B](#) and [C](#)). This indicates that the motors wait on the same protofilaments as used for approaching the roadblock. In contrast, the starting events were associated with significant transverse shifts in $\sim 70\%$ of the cases ($69 \pm 10\%$, mean \pm SD, $N = 3$ roadblock concentrations, [Table S4](#)). We found that the significant transverse shifts resembled a symmetric distribution that 1) peaked at around ± 10 nm and 2) showed equal probabilities toward the left and right directions (*red bars* in [Fig. 3 D](#)). This indicates that the motors can circumvent roadblocks on either side by small transverse shifts. We note that the same circumvention mechanism may have been at play for the insignificant transverse shifts where the side-shifting may have been obscured by the MT-motor geometry, i.e., when motors were stepping on the sides of the MTs.

Averaging the longitudinal displacements of the AuNPs during 10 ms before and 10 ms after the starting events allowed us to calculate the longitudinal shifts ([Fig. 3 C](#), [Material and Methods](#)). We found that the majority of longitudinal shifts were biased into the forward direction (69%), perhaps with multiples of 8 nm ([Fig. 3 E](#)). 14% of the starting events were associated with large longitudinal shifts of $> \pm 25$ nm. Subdividing the longitudinal shifts into shifts associated with significant transverse shifts to the left and right as well as insignificant transverse shifts allows the visualization of the directional aspect of the circumvention process in a heat map ([Fig. 3 F](#)). Color coding the number of shifts performed toward a certain location indicates that various neighboring tubulin dimers are used as motor binding sites alternative to the roadblocked tubulin dimer on the same protofilament.

In agreement with the results for GFP-labeled motors, we found similar waiting times of the AuNP-loaded motors (0.39 ± 0.04 s, mean \pm SD, $N = 3$ roadblock conditions),

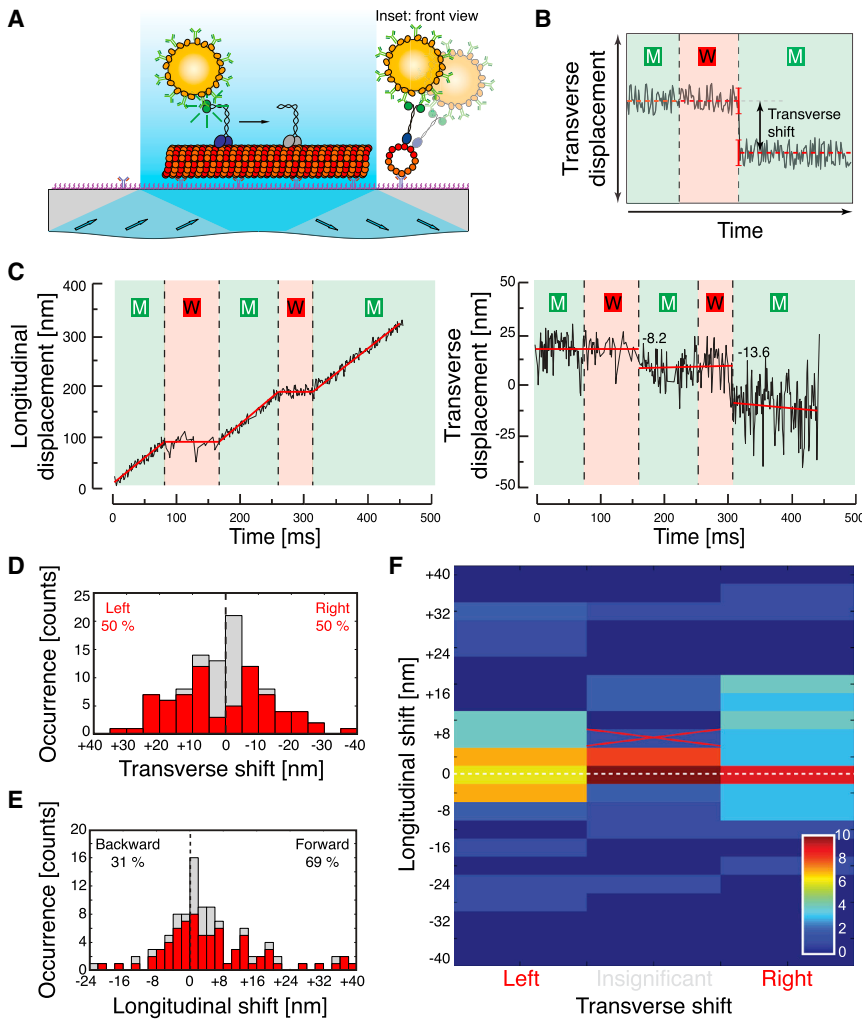


FIGURE 3 Investigation of the mechanism by which motors circumvent roadblocks. (A) Individual AuNP-loaded motors (coupled via GFP-antibodies to GFP-labeled motor tails) were allowed to interact with surface-immobilized, roadblock-decorated MTs in the presence of 1 mM ATP. (Inset) Switching between MT protofilaments requires the motor head to move sideways by ~ 6 nm, whereas the accompanied transverse shift of the AuNP is amplified by the extended motor tail and the AuNP diameter. (B) The transverse shift is determined by the difference in transverse displacement associated with stopping and starting events. Waiting phases (W, underlined red) and moving phases (M, underlined green) were deduced from the longitudinal displacement (see C, left). (C) Exemplary trajectory of a pausing motor: longitudinal (left) and transverse displacement (right) versus time. The sizes of the transverse shifts are given for each starting event. A negative shift depicts movements toward the right. (D) Histogram of transverse shifts ($N = 106$ starting events from pausing motors). Contributions by significant and insignificant shifts are shown in red and gray, respectively. (E) Histogram of longitudinal shifts (corresponding to the events in D). Contributions from events with significant and insignificant transverse shifts are shown in red and gray, respectively. (F) Heat map of longitudinal shifts sorted into shifts associated with significant transverse shifts to the left and right as well as insignificant transverse shifts (corresponding to D and E). The dashed white line denotes the longitudinal displacement before the circumvention event and the red cross denotes the presumed longitudinal position of the roadblock.

which were not significantly different for the three roadblock conditions ($p > 0.4$, Welch's unpaired t -test, Fig. S9). Moreover, also consistent with the results for the GFP-labeled motors, we found that upon increasing the roadblock concentration, the fraction of moving motors decreased, whereas the fraction of stopping, starting, pausing, and waiting motors increased (Table S3). Notwithstanding, AuNP-loaded motors showed a higher roadblock circumvention probability ($51 \pm 2\%$, mean \pm SD, $N = 3$) compared to GFP-labeled motors (28%, see above). For the range of concentrations tested here, this probability was independent of the density of roadblocks. Detailed explanations and analyses of the behavior of AuNP-loaded motors upon encountering roadblocks are provided in Fig. 4 and Table S4.

DISCUSSION

We found that the mean velocity, mean run length, and the mean dwell time of kinesin-1 motors decreased in the presence of permanent roadblocks. Although these findings are in qualitative agreement with previous publications

(12–15), we here additionally accessed the roadblock spacing by calibrating the fluorescence of GFP-labeled roadblocks along MTs to the concentration of roadblocks added during incubation. We found that at higher roadblock concentrations the mean run length converged toward the mean roadblock spacing (see Fig. 2 B) indicating that roadblocks primarily trigger the detachment of motors from the MTs. Hence, the roadblocks act as barriers limiting the free paths of the motors on the MTs. The presence of roadblocks also caused the motors to exhibit a significant number of waiting phases in their trajectories. Interestingly, the mean waiting time of the motors was independent of the roadblock concentration (see Fig. 1 C), indicating that waiting phases are an intrinsic property of individual motor-roadblock encounters. This waiting time of ~ 0.4 s corresponds to a motor off-rate in front of a roadblock of 2.5 s^{-1} , which is \sim threefold higher than the off-rate for unimpeded motor movement of 0.9 s^{-1} . If we assume that kinesin-1 waits in a one-head-bound state we can interpret the waiting time by a 40-fold deceleration of the detachment of the bound head compared to unimpeded stepping (0.01 s per forward

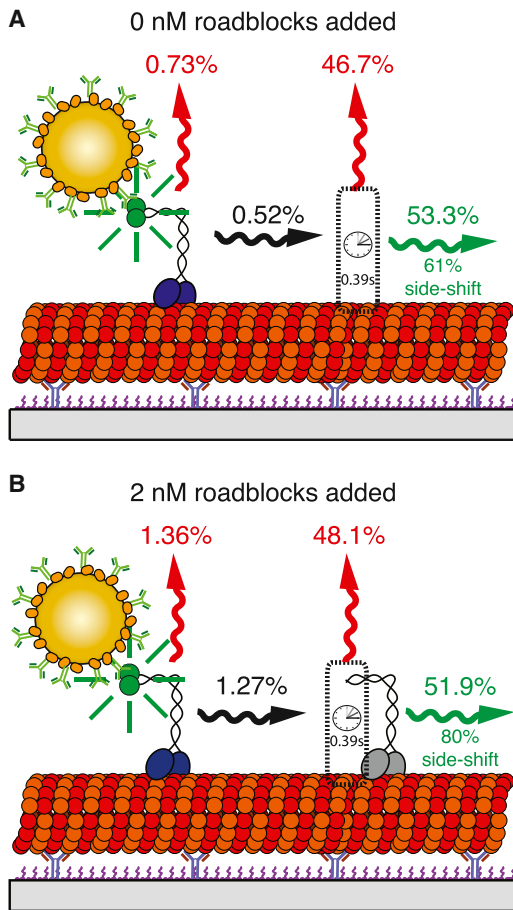


FIGURE 4 Behavior of AuNP-loaded kinesin-1 motors in the absence and presence of 2 nM added roadblocks. (A) In the absence of added roadblocks (at 0 nM roadblocks), motors detached with a probability of 0.73% per step. Upon encounter of an intrinsic obstacle (dotted box, here with a probability of 0.52% per step), motors switched into a waiting phase lasting on average 0.39 s. Subsequently, motors either detached in 46.7% of the cases or continued to walk with a chance of 53.3% of the cases. Circumvention events were accompanied by significant transverse shifts in 61% of the cases. (B) In the presence of 2 nM added roadblocks, motors detached with a 1.9-fold higher probability (1.36% per step). Roadblocks were encountered with a 2.4-fold higher probability (1.27% per step) but the duration of waiting phases remained unchanged (0.39 s). Waiting phases were exited by detachment in 48.1% and by continuation of walking in 51.9%. Circumvention events were accompanied by significant transverse shifts in 80% of the cases. See [Table S4](#) for the full analysis including the condition of 4 nM added roadblocks. To see this figure in color, go online.

step). This deceleration factor is \sim twofold larger than reported by Telley et al. (13) and >15 -fold larger compared to Crevel et al. (12). These differences may originate from different motor constructs (kinesin-1 from *Drosophila melanogaster* in (13) instead of *Rattus norvegicus*) and different ionic buffer strengths (BRB12 in (12) instead of BRB80). Moreover, Crevel et al. (12) worked at conditions where the binding sites on the MTs were saturated with roadblocks and motors. In such a restricted environment, the immediate detachment of the motors might become predominant. After the waiting phases, we observed that \sim 30%

of the GFP-labeled motors and \sim 50% of the AuNP-loaded motors started to move again, presumably by circumventing a roadblock. Although the existence of extended waiting phases has been observed earlier (13,14), the possibility to circumvent roadblocks was only a subject of speculation (10,13,15–17).

By performing numerical simulations, we found that the experimentally observed motility parameters could be readily reproduced when considering the finite waiting time and circumvention probability of individual motors. Even more convincingly, shortening the waiting time to 0 s and/or reducing the circumvention probability to 0% caused disagreement between experimental and simulated data. Interestingly, however, the capability to circumvent roadblocks gained the motors only an additional run length of 64 ± 20 nm (mean \pm SD, $N = 6$ roadblock conditions, compare *green* and *orange* lines in Fig. 2 B). This rather small effect can be explained by the fact that motors, which have circumvented a roadblock, soon encounter another roadblock. Thus, run lengths significantly longer than the mean roadblock spacing can only be expected for very high roadblock circumvention probabilities. In fact, when performing our simulations with a circumvention probability of 100% we found the mean run length to become independent of the roadblock density.

To gain insight into the detailed mechanism by which motors circumvent roadblocks, we loaded 40 nm AuNPs to the GFP-labeled tails of kinesin-1 and directly imaged the circumvention process with nanometer precision and millisecond resolution. Associated with a starting event we found transverse shifts of mostly about ± 10 nm (Fig. 3 D). This is almost twice the distance between neighboring protofilaments but can be explained by the long kinesin-1 tail (contour length \sim 32.5 nm), which amplified the interprotofilament distances in conjunction with the three-dimensional MT-motor geometry (see [Supporting Material E](#) and Fig. S10). Because transverse shifts larger than ± 40 nm were observed in only $<10\%$ of the cases, we argue that side-shifts mainly originated from transitions between adjacent protofilaments rather than between further spaced protofilaments, as speculated by Dreblow et al. (15).

An interesting finding of our study is that side-shifts toward the left and right protofilament were equally likely. This is in agreement with Yildiz et al. (25), who studied the movement of kinesin-1 motors—notably in the absence of roadblocks—by labeling the motor heads with quantum dots. The high frequency of sidesteps in their study (up to 13% per forward step, not necessarily associated with a waiting phase) may have been caused by an interference of the quantum dots (diameter of \sim 20 nm) with the stepping of the motor heads. The frequency for side-shifting without a prior waiting phase was >50 -fold lower in our case ($<0.2\%$ per forward step, see [Table S4](#)), where motors were labeled at the tails, i.e., away from the motor heads. Our data indicate that the protofilament tracking mechanism

of kinesin-1 is strong but not ultimately strict, causing the molecule to switch protofilaments on average every 500 forward steps ($= 4 \mu\text{m}$). This finding is in agreement with Nitzsche et al. (26), who studied kinesin-1-based transport of supertwisted, quantum dot-labeled 14-protofilament MTs in gliding motility assays using fluorescence interference contrast microscopy. They showed that MTs were rotated with a pitch of $7.9 \pm 1.4 \mu\text{m}$. Interestingly, a similar spread of $\sim \pm 1.2 \mu\text{m}$ in the rotational pitches can be explained by an unbiased side-shifting probability of 0.2% causing the motors to perform approximately two one-protofilament side-shifts toward either side per full MT rotation. Additional evidence for unbiased side-shifting comes from rotation experiments (similar to (26)) with roadblock-decorated MTs where the rotational pitch was found to be independent of the presence of roadblocks (A. Mitra, B CUBE—Center for Bioengineering, Technische Universität Dresden, personal communication, 2014).

What is the origin of the observed side-shifting upon roadblock encounters? Although our results do not rule out the possibility that individual kinesin-1 motors directly side-step to neighboring MT protofilaments during a processing run, our data suggest the involvement of motor unbinding and rebinding for the following reasons. First, the waiting times at a roadblock were the same for detachment and circumvention events, rendering it likely that unbinding of the motors triggered the circumvention events. Second, the circumvention probability was higher for the AuNP-loaded motors as compared to the unloaded (GFP-labeled) motors. This behavior may originate from a higher rebinding probability of the loaded motors as the AuNPs are expected to slow down motor diffusion after unbinding. Third, recent studies indicate that the neck-linker of kinesin-1 is designed short-enough to exclusively reach the forward binding sites (27,28). In contrast, we found a wide range of longitudinal shifts associated with the starting events. In particular, $\sim 14\%$ of the longitudinal shifts were larger than $\pm 25 \text{ nm}$ and can certainly not be explained by a direct stepping mechanism. Along these lines Hoepflich et al. (10) recently reported that the motility of kinesin-2, having a longer neck-linker than kinesin-1 (17 and 14 amino acids, respectively), remained relatively unaffected upon addition of tau acting as obstacles on the MT. However, in contrast to the rigor-binding kinesin-1 mutants used as roadblocks in our study, tau diffuses on MTs (11) and interacts preferentially with the α -tubulin subunit (29) which makes the two studies not directly comparable. Nevertheless, the shifting pattern of the starting events (see Fig. 3 F and the geometrical considerations in Supporting Material E) speaks in favor of roadblock circumvention being a rather local process, taking place on length scales of only a few tens of nanometers.

Although not much data on the concentration or density of MAPs at physiological conditions are available, one study determined the tau/tubulin ratio in neurons to vary between 0.025 and 0.05, corresponding to $1 \mu\text{M}$ tau per $20 \mu\text{M}$ to

$40 \mu\text{M}$ polymerized tubulin (30). Such values correspond to mean roadblock spacings of $\sim 300 \text{ nm}$ along a single protofilament; values which were covered in our experiments (see Fig. 2 B, dotted line). Admittedly, most native obstacles are likely to bind to MTs in a transient and/or diffusive manner. This renders their interaction with motors more intricate as they may also get removed or pushed aside by the motors. Our studies performed with static, permanent roadblocks may thus not be universally applicable to all obstacles, however, will bear relevance for some of them among which are inactive motors (31).

CONCLUSIONS

What is the physiological relevance of roadblock circumvention after a waiting phase? Although the mean run length of kinesin-1 appears to increase only slightly, the finite waiting phase may be quite relevant. Waiting phases occur when kinesin-1 encounters an obstacle blocking the next tubulin dimer. In this case the leading head of the motor cannot bind immediately, and the trailing head cannot detach. This keeps the motor in the waiting phase, which is only ceased by detachment of the trailing head and rebinding to an alternative binding site. The suppression of detachment might be beneficial for robust cargo transport in vivo where small teams of motors work together (7,32,33). Waiting of one motor may allow other cargo-bound motors to engage into the job of transportation and therefore prevent the interruption of cargo delivery. It can be speculated whether motor proteins with longer neck-linkers, such as kinesin-2 (10) and kinesin-8 (27), might use shorter waiting phases when confronted with roadblocks, because bypassing an obstacle via direct side-stepping to an adjacent protofilament is more likely. For individual kinesin-8 motors, in particular, reaching the MT end even under crowded conditions is crucial to its function as length-dependent MT depolymerase.

SUPPORTING MATERIAL

Supporting Materials and Methods, eleven figures, and four tables are available at [http://www.biophysj.org/biophysj/supplemental/S0006-3495\(15\)00310-0](http://www.biophysj.org/biophysj/supplemental/S0006-3495(15)00310-0).

ACKNOWLEDGMENTS

We thank Corina Bräuer, Cornelia Thodte, and the Antibody-Facility at the Max Planck Institute of Molecular Cell Biology and Genetics Dresden for technical support, as well as Oliver Wüseke for contributions to initial experiments.

We acknowledge financial support from the European Research Council (starting grant 242933, NanoTrans), the European Social Funds (grant 100111059, MindNano and grant 100107464, ChemIT), the German Research Foundation (Cluster of Excellence Center for Advancing Electronics Dresden and the Heisenberg Program) as well as the Max Planck Society and the Technische Universität Dresden.

REFERENCES

- Fletcher, D. A., and J. A. Theriot. 2004. An introduction to cell motility for the physical scientist. *Phys. Biol.* 1:T1–T10.
- Chevalier-Larsen, E., and E. L. F. Holzbaur. 2006. Axonal transport and neurodegenerative disease. *Biochim. Biophys. Acta.* 1762:1094–1108.
- Stokin, G. B., and L. S. B. Goldstein. 2006. Axonal transport and Alzheimer's disease. *Annu. Rev. Biochem.* 75:607–627.
- Stokin, G. B., C. Lillo, ..., L. S. Goldstein. 2005. Axonopathy and transport deficits early in the pathogenesis of Alzheimer's disease. *Science.* 307:1282–1288.
- Prusiner, S. B. 2012. Cell biology. A unifying role for prions in neurodegenerative diseases. *Science.* 336:1511–1513.
- Trinczek, B., A. Ebner, ..., E. Mandelkow. 1999. Tau regulates the attachment/detachment but not the speed of motors in microtubule-dependent transport of single vesicles and organelles. *J. Cell Sci.* 112:2355–2367.
- Vershini, M., B. C. Carter, ..., S. P. Gross. 2007. Multiple-motor based transport and its regulation by Tau. *Proc. Natl. Acad. Sci. USA.* 104:87–92.
- Seitz, A., H. Kojima, ..., E. Mandelkow. 2002. Single-molecule investigation of the interference between kinesin, tau and MAP2c. *EMBO J.* 21:4896–4905.
- Dixit, R., J. L. Ross, ..., E. L. F. Holzbaur. 2008. Differential regulation of dynein and kinesin motor proteins by tau. *Science.* 319:1086–1089.
- Hoepflich, G. J., A. R. Thompson, ..., C. L. Berger. 2014. Kinesin's neck-linker determines its ability to navigate obstacles on the microtubule surface. *Biophys. J.* 106:1691–1700.
- Hinrichs, M. H., A. Jalal, ..., T. Scholz. 2012. Tau protein diffuses along the microtubule lattice. *J. Biol. Chem.* 287:38559–38568.
- Crevel, I. M.-T., M. Nyitrai, ..., R. A. Cross. 2004. What kinesin does at roadblocks: the coordination mechanism for molecular walking. *EMBO J.* 23:23–32.
- Telley, I. A., P. Bieling, and T. Surrey. 2009. Obstacles on the microtubule reduce the processivity of Kinesin-1 in a minimal in vitro system and in cell extract. *Biophys. J.* 96:3341–3353.
- Korten, T., and S. Diez. 2008. Setting up roadblocks for kinesin-1: mechanism for the selective speed control of cargo carrying microtubules. *Lab Chip.* 8:1441–1447.
- Dreblow, K., N. Kalchishkova, and K. J. Böhm. 2010. Kinesin passing permanent blockages along its protofilament track. *Biochem. Biophys. Res. Commun.* 395:490–495.
- Tarhan, M. C., Y. Orazov, ..., H. Fujita. 2013. Biosensing MAPs as "roadblocks": kinesin-based functional analysis of tau protein isoforms and mutants using suspended microtubules (sMTs). *Lab Chip.* 13:3217–3224.
- Schmidt, C., B. Kim, ..., V. Vogel. 2012. Tuning the "roadblock" effect in kinesin-based transport. *Nano Lett.* 12:3466–3471.
- Schneider, R., T. Glaser, ..., S. Diez. 2013. Using a quartz paraboloid for versatile wide-field TIR microscopy with sub-nanometer localization accuracy. *Opt. Express.* 21:3523–3539.
- Rogers, K. R., S. Weiss, ..., R. Cross. 2001. KIF1D is a fast non-processive kinesin that demonstrates novel K-loop-dependent mechanochemistry. *EMBO J.* 20:5101–5113.
- Ruhnow, F., D. Zwicker, and S. Diez. 2011. Tracking single particles and elongated filaments with nanometer precision. *Biophys. J.* 100:2820–2828.
- Thorn, K. S., J. A. Ubersax, and R. D. Vale. 2000. Engineering the processive run length of the kinesin motor. *J. Cell Biol.* 151:1093–1100.
- Mashanov, G. I., D. Tacon, ..., J. E. Molloy. 2004. The spatial and temporal dynamics of pleckstrin homology domain binding at the plasma membrane measured by imaging single molecules in live mouse myoblasts. *J. Biol. Chem.* 279:15274–15280.
- Nakata, T., and N. Hirokawa. 1995. Point mutation of adenosine triphosphate-binding motif generated rigor kinesin that selectively blocks anterograde lysosome membrane transport. *J. Cell Biol.* 131:1039–1053.
- Korten, T., B. Nitzsche, ..., S. Diez. 2011. Fluorescence imaging of single Kinesin motors on immobilized microtubules. *Methods Mol. Biol.* 783:121–137.
- Yildiz, A., M. Tomishige, ..., R. D. Vale. 2008. Intramolecular strain coordinates kinesin stepping behavior along microtubules. *Cell.* 134:1030–1041.
- Nitzsche, B., F. Ruhnow, and S. Diez. 2008. Quantum-dot-assisted characterization of microtubule rotations during cargo transport. *Nat. Nanotechnol.* 3:552–556.
- Bormuth, V., B. Nitzsche, ..., S. Diez. 2012. The highly processive kinesin-8, Kip3, switches microtubule protofilaments with a bias toward the left. *Biophys. J.* 103:L4–L6.
- Grant, B. J., D. M. Gheorghe, ..., R. A. Cross. 2011. Electrostatically biased binding of kinesin to microtubules. *PLoS Biol.* 9:e1001207.
- Santarella, R. A., G. Skiniotis, ..., A. Hoenger. 2004. Surface-decoration of microtubules by human tau. *J. Mol. Biol.* 339:539–553.
- Mandelkow, E. M., and E. Mandelkow. 2012. Biochemistry and cell biology of tau protein in neurofibrillary degeneration. *Cold Spring Harb. Perspect. Med.* 2:a006247.
- Scharrel, L., R. Ma, ..., S. Diez. 2014. Multimotor transport in a system of active and inactive kinesin-1 motors. *Biophys. J.* 107:365–372.
- Shubeita, G. T., S. L. Tran, ..., S. P. Gross. 2008. Consequences of motor copy number on the intracellular transport of kinesin-1-driven lipid droplets. *Cell.* 135:1098–1107.
- Soppina, V., A. K. Rai, ..., R. Mallik. 2009. Tug-of-war between dissimilar teams of microtubule motors regulates transport and fission of endosomes. *Proc. Natl. Acad. Sci. USA.* 106:19381–19386.